

Personalized Modeling and Assessment of the Aortic-Mitral Coupling from 4D TEE and CT

Razvan Ioan Ionasec^{1,4} *, Ingmar Voigt^{2,5}, Bogdan Georgescu¹, Yang Wang¹, Helene Houle³, Joachim Hornegger⁵, Nassir Navab⁴, and Dorin Comaniciu¹

¹ Integrated Data Systems, Siemens Corporate Research, Princeton, USA

² Software and Engineering, Siemens Corporate Technology, Erlangen, Germany

³ Ultrasound, Siemens Medical Solutions, Mountain View, CA, USA

⁴ Computer Aided Medical Procedures, Technical University Munich, Germany

⁵ Chair of Pattern Recognition, Friedrich-Alexander-University, Erlangen, Germany

Abstract. The anatomy, function and hemodynamics of the aortic and mitral valves are known to be strongly interconnected. An integrated quantitative and visual assessment of the aortic-mitral coupling may have an impact on patient evaluation, planning and guidance of minimal invasive procedures. In this paper, we propose a novel model-driven method for functional and morphological characterization of the entire aortic-mitral apparatus. A holistic physiological model is hierarchically defined to represent the anatomy and motion of the two left heart valves. Robust learning-based algorithms are applied to estimate the patient-specific spatial-temporal parameters from four-dimensional TEE and CT data. The piecewise affine location of the valves is initially determined over the whole cardiac cycle using an incremental search performed in marginal spaces. Consequently, efficient spectrum detection in the trajectory space is applied to estimate the cyclic motion of the articulated model. Finally, the full personalized surface model of the aortic-mitral coupling is constructed using statistical shape models and local spatial-temporal refinement. Experiments performed on 65 4D TEE and 69 4D CT sequences demonstrated an average accuracy of 1.45mm and speed of 60 seconds for the proposed approach. Initial clinical validation on model-based and expert measurement showed the precision to be in the range of the inter-user variability. To the best of our knowledge this is the first time a complete model of the aortic-mitral coupling estimated from TEE and CT data is proposed.

1 Introduction

Aortic and mitral valves are the most commonly diseased valves, cumulating in 64 percent and 14 percent, respectively of the valvular heart disease case. The coupling of the aortic and mitral valvular annuli through fibrous tissue is evident and leads to strong functional and hemodynamical interdependency. Recent studies and findings demand that the dynamics and morphologies of the aortic

* Correspondence to razvan.ionasec@siemens.com

and mitral valve must be considered simultaneously [1, 2]. Reciprocal changes of the aortic and mitral annular areas have been reported and it was concluded, that the fibrous aortic-mitral continuity acts as an anchor for the valves. Together with the muscular portions of either annuli and their contraction during their reciprocal motion, it facilitates the opening and closing of the other valve during systole and diastole respectively [3]. Various findings and facts related to interventions on both valves emphasize the notion of their coupling. In transapical aortic valve replacement, the prosthesis’s stent must not be placed too far downwards into the directions of the left ventricle, as it would impair the mitral anterior leaflet’s mobility [4]. Moreover another recent study pointed out, that mitral regurgitation can be positively affected by aortic valve replacement [5]. Understanding the dynamics and morphology of the aortic-mitral valvular apparatus is important as a base for diagnosis and treatment decisions, optimal design of prostheses and intervention outcome improvement.

Recently, personalized valve models have attracted great attention and are expected to significantly advance the management of patients with valve heart disease. To date, separate approaches were reported for modeling of both valves [6, 7]. Veronesi *et al.*[3] reported a method, where both annuli were segmented with manual initialization and quantified. Up to now the full joint morphology and dynamics of both valves at the same time have not been studied due to the lack of suitable methods and tools.

In this paper we propose a new model driven approach for quantitative and visual assessment of the aortic-mitral complex, which models all relevant anatomical structures of both valves. For the first time a complete personalized model of the aortic-mitral coupling, non-invasively derived from 4D Computed Tomography (CT) and 4D Transoesophageal Echocardiography (TEE) acquisitions, accurately represents the valves’ morphology and function. The personalized parameter estimation from input image sequences is performed efficiently using a robust and hierarchical learning-based algorithm. Our approach enables for integrated quantification, and has the potential to fuel research on mixed valve disease, cardiac pathophysiology and interventional procedures.

2 Physiological Modeling of the Aortic-Mitral coupling

We propose a physiological model of the complete aortic-mitral apparatus capable to capture complex morphological, dynamic and pathological variations. The valves are coupled by a fibrous tissue [1] and work in synchrony [3, 2] to regulate the blood flow in the left heart. The central anatomical structures are: aortic root and leaflets along with mitral anterior and posterior leaflets. To efficiently handle the anatomical complexity, the model representation and corresponding parameterization is constructed hierarchically and includes: a global piecewise affine model, a non-rigid articulated model and a full surface model.

The time dependent global position (c_x, c_y, c_z, t) , orientation $(\alpha_x, \alpha_y, \alpha_z, t)$ and scale (s_x, s_y, s_z, t) , are defined for each valve individually and illustrated as bounding boxes in Fig. 1. Positions are given by the valve’s barycenters, while

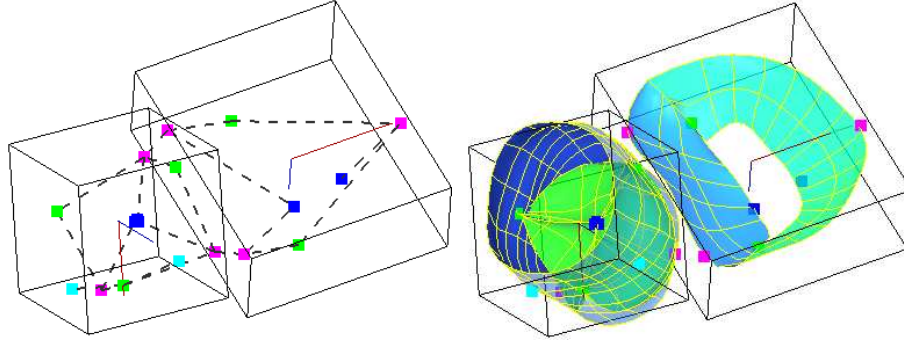


Fig. 1. Physiological model of the aortic-mitral coupling. **Left:** Non-rigid articulated model including the following landmarks: aortic and mitral commissures (green), aortic and mitral tips (blue), aortic hinges and mitral triagones (magenta) and coronary ostia (cyan). **Right:** Full surface model: aortic root (blue), aortic leaflets (green), anterior (light-blue) and posterior (light green) mitral leaflets.

scales are chosen to comprise the entire underlying anatomy. The long axes are defined by the normal vectors to the aortic-commissural plane and mitral-trigonal plane, while short axes point from the barycenters to the LR-commissure and mitral posteroannular midpoint, respectively.

The aortic and mitral valves execute a rapid opening-closing movement, which follows a complex and synchronized motion pattern. Normalized by the global parameters, the non-rigid motion is represented through an articulated model. It consists of 18 joints, which are relevant anatomical landmarks (see Fig. 1 **Left**). Each joint j is parameterized through the corresponding trajectory \mathbf{a}_j , given by the concatenation of the spatial coordinates, $\mathbf{a}^j(t) \in \mathbb{R}^3$, over time $t = 0, \dots, n - 1$:

$$\mathbf{a}^j = [\mathbf{a}^j(0), \mathbf{a}^j(1), \dots, \mathbf{a}^j(t), \dots, \mathbf{a}^j(n - 1)] \quad (1)$$

The highest abstraction layer models the 3D surfaces of the anatomical structures: aortic root, left/right/none coronary leaflets for the aortic valve, and anterior/posterior leaflets for the mitral valve (see Fig. 1 **Right**). The aortic root connects the ascending aorta to the left ventricle outflow tract and is modeled as a cylindrical surface constrained by the hinges, coronary ostia and aortic commissures. Attached to the root are the three aortic leaflets, delineated by the corresponding tip, hinge and commissures, and modeled as paraboloids. The anterior and posterior leaflets of the mitral valve separate hemodynamically the left ventricle from the left atrium. The aortic mitral curtain, which anatomically links the two valves, ends into the left and right fibrous trigones. These, together with the mitral-commissures and corresponding tip are fixing the anterior leaflet. The posterior leaflet, divided into three scallops, is located between the mitral commissures, middle triagone and its corresponding tip. The saddled shaped mitral annulus is modeled implicitly by the upper margins of the mitral leaflets. For

each structure k , all surfaces $C^k(u, v, t)$ are parameterized by spatial coordinates u, v and time t and represented by Non uniform rational B-splines (NURBS) [8]. The temporal parameter t extends the standard NURBS surface equation by applying the tensor product, and is used to capture the temporal variation over the cardiac cycle. The surface model is anchored to the articulated model introduced above and is constraint by anatomically-driven boundary condition to form a full 4D physiological aortic-mitral model.

3 Robust Estimation of Personalized Model

The model parameters introduced in section 2 are estimated from 4D patient specific data to obtain a personalized representation of the aortic-mitral apparatus. To maximize efficiency and comply with the hierarchical model definition, the estimation algorithm is based on robust learning methods and is divided in three stages: Global Localization and Motion Estimation, Trajectory Spectrum Learning and Dynamic Surface Model Fitting.

Global Localization and Motion Estimation - The global location and motion is represented by the 3D+t affine parameters $(c_x, c_y, c_z, \alpha_x, \alpha_y, \alpha_z, s_x, s_y, s_z, t)$, for each valve. These are estimated by combining anatomy detectors trained using the Marginal Space Learning (MSL) framework [9] with a variant of the Random Sample Consensus (RANSAC) [10]. MSL provides an efficient way of learning high dimensional models and fast online search by operating in subspaces of increasing dimensionality. Anatomical classifiers are sequentially learned on the subspaces: position, position + orientation and position + orientation + scale. The probabilistic boosting tree (PBT) [11], in combination with Haar and Steerable Features [9], is applied for training. The RANSAC estimator is employed to obtain a robust and time consistent global motion. Several high-probable hypotheses are obtained for each frame by scanning the trained MSL-based affine estimator over the input image sequence. Assuming a constant global motion, the candidate hypotheses are sequentially sampled as the current motion model parameters and the best fit from each frame is considered when computing the robust quality measure. The final inlier selection is given by the model with the maximum number of hypotheses within the pre-specified tolerance $\sigma = 7mm$, measured using the L1 norm.

Trajectory Spectrum Learning - We propose a novel algorithm to estimate the non-rigid motion of the articulated model by performing learning and optimization in trajectory spectrum spaces [12]. The trajectory of each joint \mathbf{a}^j in (1) can be represented by its corresponding discrete Fourier transform (DFT) coefficients:

$$\mathbf{s}^j(f) = \sum_{t=0}^{n-1} \mathbf{a}^j(t) e^{\frac{-j2\pi t f}{n}} \quad (2)$$

where $\mathbf{s}^j(f)$ is the frequency spectrum of the x , y , or z components of the trajectory $\mathbf{a}^j(t)$, and $f = 0, 1, \dots, n - 1$. Consequently, the objective to find the trajectory \mathbf{a}^j , with the maximum posterior probability for a series of volumes I can be expressed as:

$$\arg \max_{\mathbf{a}^j} p(\mathbf{a}^j|I) = \arg \max_{\mathbf{s}^j} p(\mathbf{s}^j|I) = \arg \max_{\mathbf{s}^j} p(\mathbf{s}^j(0), \dots, \mathbf{s}^j(n-1)|I(0), \dots, I(n-1)) \quad (3)$$

As the original search space is high dimensional, the learning and optimization is performed efficiently in orthogonal subspace with increased dimensionality spanned by the DFT bases functions. This incremental approach initially captures coarse level motion and gradually refines high-frequency deformations as the search space dimension increases. Starting with the initial space of the DC ($\mathbf{s}^j(0)$), we iteratively add frequency components $\mathbf{s}^j(f)$ and learn the posterior probability in each subsequent subspace until reaching the dimensionality of the original space, $n - 1$. At a certain stage i , the subspace includes the spectrum component $\mathbf{s}^j(0), \dots, \mathbf{s}^j(i)$ and the conditional probability is modeled by a trained detector D_i :

$$p(\mathbf{s}^j(i)|\mathbf{s}^j(0), \dots, \mathbf{s}^j(i-1)) = D_i(\mathbf{s}^j(0), \dots, \mathbf{s}^j(i)) \quad (4)$$

For each subspace, the detectors D_i are trained on positive and negative trajectories extracted from the training set, using the probabilistic boosting tree (PBT) algorithm in conjunction with steerable features [9].

The detection starts with a zero-spectrum and estimates incrementally the amplitude and phase of each DFT component $\mathbf{s}^j(f)$. At a certain stage i , high probability hypotheses are determined and preserved by D_i . Subsequently, the dimensionality of the search subspace is extended to $i + 1$ with the spectrum component $\mathbf{s}^j(i + 1)$ and the detection is repeated using D_{i+1} . The algorithm stops when the original space is reached and outputs the optimal trajectory spectrum ($\mathbf{s}^j(0), \dots, \mathbf{s}^j(n - 1)$). The location and motion of the model is obtained by reconstructing the trajectory \mathbf{a}^j of each joint j applying the inverse DFT transformation⁶. The spectrum representation and corresponding decomposition enable efficient motion learning and optimization as the number of tested hypotheses during detection is significantly reduced by at least on magnitude.

Dynamic Surface Model Fitting - The full surface model is initialized by fitting the mean shape, learned from the training set, to the estimated articulated model from the previous section. Boundary detectors, trained using PBT and steerable features, deform locally the surfaces to obtain proper object delineation [9]. The resulting surfaces are projected on the corresponding shape space to impose the geometric smoothness constraint. The PCA-based shape

⁶ The non-rigid motion trajectories are reconstructed from the real coefficients of the DFT, while optimization runs in the complex space, considering both amplitude (real) and phase (imaginary)

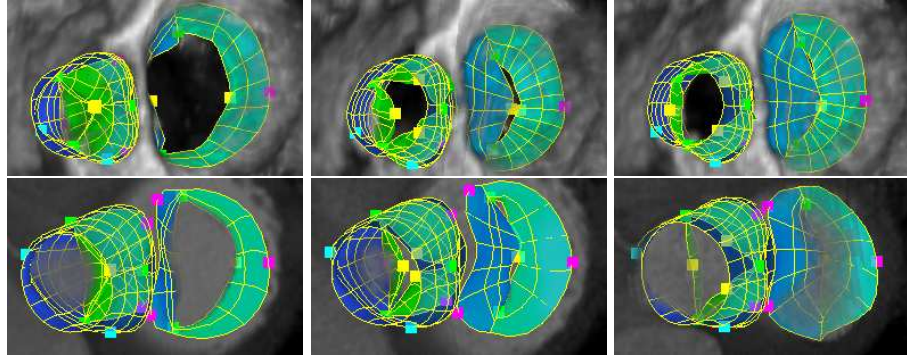


Fig. 2. Examples of the personalized model in TEE (**Top**) and CT (**Bottom**).

model, which contains 80 modes, is computed from point correspondences maintained by model re-sampling within anatomical local coordinates (Sec. 2). To enhance temporal smoothness, a learned motion prior, combined with optical flow estimation, is applied to predict the propagated surfaces based on the previous frames [13]. The above procedure is repeated for each volume in the image sequences, in both forward and backward directions, to obtain a personalized dynamic surface model of the entire aortic-mitral apparatus.

4 Results

The proposed method for personalized aortic-mitral modeling was evaluated on 69 4D CT (690 volumes) and 65 4D TEE (1516 volumes) studies. The data set contains healthy as well as valves affected by various diseases, such as stenosis, regurgitation, prolapse and annular dilation. Both CT and TEE scans were acquired using heterogeneous protocols with various sizes and resolutions. Each study is associated with a manual performed annotation, which represents the ground-truth. This was obtained and refined together with clinical experts while gradually improving the semi-automated annotation system. Performance is reported on three-fold cross validation experiments.

The accuracy of the algorithm for the three estimation stages is presented in Table 1. Global location and motion parameters were estimated on low-resolution (3mm) images, with errors measured from the Euclidean distance of the bounding boxes' corner points between ground-truth and detected results. The accuracy of the non-rigid articulated model estimator is computed from the average Euclidean distance over all aortic and mitral joints. Performance for the full surface estimator is measured by the point-to-mesh distance. We obtain an average accuracy of 1.45 mm with a total computation time of 60 seconds for the personalized aortic-mitral coupling model (see Fig.2). The obtained system-error is compared to the inter-user variability in an experiment involving a randomly

Table 1. Errors for each detection stage in TEE (**Left**) and CT (**Right**).

	(mm)	Mean	Std.	Median	80%	Mean	Std.	Median	80%
Global Affine Parameters		6.95	4.12	5.96	8.72	8.09	3.32	7.57	10.4
Non-Rigid Articulated Model		3.78	1.55	3.43	4.85	2.93	1.36	2.59	3.38
Full Surface Model		1.54	1.17	1.16	1.78	1.36	0.93	1.30	1.53

selected subset of 10 TEE sequences and models placed manually by 3 expert users. The barycentric distance and angle between the aortic and mitral valve were measured from the model in end-diastole and end-systole. Fig. 3 demonstrates that the system-error relative to the mean measurements of all experts lies for 90% of the cases within the 80% user-variability confidence interval.

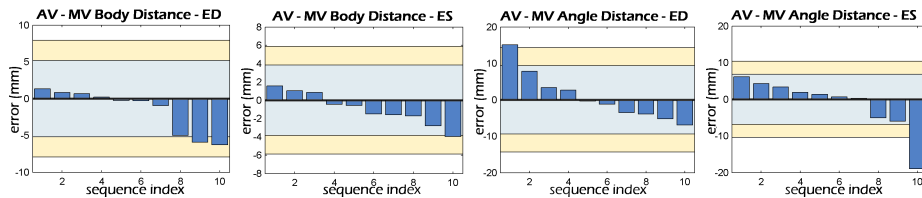


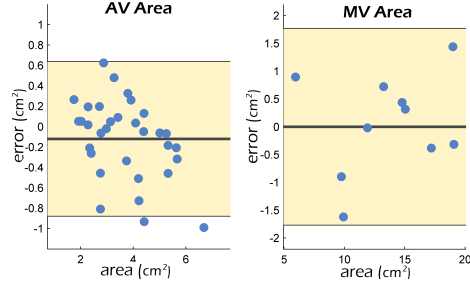
Fig. 3. System error compared to the inter-user variability. The sorted system error (blue bars) and the 80% (light blue area) and 90% (yellow) confidence intervals of the user variability determined from the standard deviation.

The inter-modality consistency of the model-based quantification was demonstrated on studies of patients which underwent both imaging investigations, TEE and cardiac CT. A strong correlation, $r=0.98$, $p<0.0001$ and 0.97-0.99 confidence intervals, was obtained on standard measurements (aortic valve area, inter-commissural distances and root diameters at the sinotubular, ventricular-arterial junction and ventricular-arterial junction), derived from the personalized model in four different CT/TEE exams.

We demonstrated the quantitative capabilities of our approach by comparing model driven to expert measurements. Table 2 presents the system-precision for various dimensions of the aortic-mitral coupling: Diameters of the ventricular-arterial junction (VAJ), sinus of valsalva (SV) and sinotubular junction (SJ), aortic valve area (AV area), mitral valve area (MV area), mitral annular circumference (AC), anteroposterior diameter (APD), anterolateral-posteromedial diameter (AL-PM-D). The mean interannular angle and interannular centroid distance were 137.0 ± 12.2 and 26.5 ± 4.2 , respectively compared to 136.2 ± 12.6 and 25.0 ± 3.2 reported in the literature [3]. Automatic, model-based quantification has the potential to advance patient evaluation, intervention planning and guidance.

Table 2. **Left:** System-precision for various dimensions of the aortic-mitral coupling. **Right:** Bland-Altman plots for the aortic and mitral valves area.

	Mean	STD
VAJ (<i>cm</i>)	0.137	0.017
SV (<i>cm</i>)	0.166	0.043
STJ (<i>cm</i>)	0.098	0.029
AC (<i>cm</i>)	0.846	0.3
APD (<i>cm</i>)	0.325	0.219
AL-PM-D(<i>cm</i>)	0.509	0.37



Pre- and post-operative modeling for a patient who underwent mitral annuloplasty revealed the substantial effect on the aortic valve (not targeted during the procedure), confirming observations from [1–3]. The aortic and mitral valvular areas over the cardiac cycle are illustrated in Fig. 4 **Left**, which clearly shows the mitral-regurgitation cured after the intervention. The synchronous annuli deformation and indirect operation effects on the aortic morphology and dynamics are illustrated in Fig. 4 **Right**.

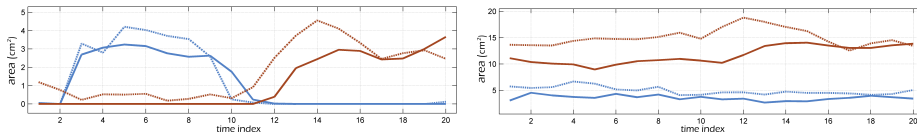


Fig. 4. Measurements obtained before (dotted lines) and after (solid lines) mitral annuloplasty. **Left:** Aortic (blue) and Mitral (red) valvular area. **Right:** Aortic (blue) and Mitral (red) annular area.

5 Discussion

Latest clinical research confirmed that the morphology, function and hemodynamic-activity of the aortic and mitral valves are strongly interconnected. In this paper, we introduced the first personalized model of the entire aortic-mitral apparatus derived from 4D TEE and 4D CT data. The full anatomy and dynamics are represented through a physiological-driven hierarchical model. From input volume sequences, we estimate the personalized parameters of the non-rigid motion and surface model by applying a robust and efficient machine learning algorithm. The presented approach enables for efficient and integrated quantification of the aortic-mitral complex. Extensive experiments performed on a large heterogeneous data set demonstrated the precision of 1.45mm and speed of 60 seconds for

the proposed approach. Furthermore, clinical validation showed a strong inter-modality and inter-subject correlation for a comprehensive set of model-based measurements. The proposed method has the potential to significantly advance the joint examination, procedure planning and prosthetic valve design for both, aortic and mitral valves.

References

1. Lansac, E., Lim, K., Shomura, Y., Goetz, W., Lim, H., Rice, N., Saber, H., Duran, C.: Dynamic balance of the aortomitral junction. *J Thorac Cardiovasc Surg* **123** (2002) 911–918
2. Timek, T., Green, G., Tibayan, F., Lai, F., Rodriguez, F., Liang, D., Daughters, G., Ingels, N., Miller, D.: Aorto-mitral annular dynamics. *Ann Thorac Surg* **76** (2003) 1944–1950
3. Veronesi, F., Corsi, C., Sugeng, L., Mor-Avi, V., Caiani, E., Weinert, L., Lamberti, C., R.M., L.: A study of functional anatomy of aortic-mitral valve coupling using 3D matrix transesophageal echocardiography. *Circ Cardiovasc Imaging* **2**(1) (2009) 24–31
4. Gessat, M., Merk, D., Falk, V., Walther, T., Noetling, A., Burgert, O.: A planning system for transapical aortic valve implantation. In: *Proc SPIE Medical Imaging*. (2009)
5. Vanden-Eynden, F., Bouchard, D., El-Hamamsy, I., Butnaru, A., Demers, P., Carrier, M., Perrault, L., Tardif, J., Pellerin, M.: Effect of aortic valve replacement for aortic stenosis on severity of mitral regurgitation. *Ann Thorac Surg* **83** (2007) 1279–84
6. Ionasec, R.I., Georgescu, B., Gassner, E., Vogt, S., Kutter, O., Scheuering, M., Navab, N., Comaniciu, D.: Dynamic model-driven quantification and visual evaluation of the aortic valve from 4d ct. In: *International Conference on Medical Image Computing and Computer-Assisted Intervention (MICCAI)*, New York (2008)
7. Voigt, I., Ionasec, R., Georgescu, B., Houle, H., Huber, M., Hornegger, J., Comaniciu, D.: Model-driven physiological assessment of the mitral valve from 4d tee. In: *Proc SPIE Medical Imaging*. (2009)
8. Piegl, L., Tiller, W.: *The NURBS book*. Springer-Verlag, London, UK (1995)
9. Zheng, Y., Barbu, A., et al.: Fast automatic heart chamber segmentation from 3d ct data using marginal space learning and steerable features. In: *International Conference on Computer Vision*. (2007)
10. Fischler, M., Bolles, R.: Random sample consensus: A paradigm for model fitting with applications to image analysis and automated cartography. *Comm. of the ACM* **24**(6) (June 1981) 381–395
11. Tu, Z.: Probabilistic boosting-tree: Learning discriminative methods for classification, recognition, and clustering. In: *International Conference on Computer Vision*. (2005) 1589–1596
12. Ionasec, R., Wang, Y., Georgescu, B., Voigt, I., Navab, N., Comaniciu, D.: Robust motion estimation using trajectory spectrum learning: Application to aortic and mitral valve modeling. In: *International Conference on Computer Vision* (submitted). (2009)
13. Yang, L., Georgescu, B., Zheng, Y., Meer, P., Comaniciu, D.: 3d ultrasound tracking of the left ventricle using one-step forward prediction and data fusion of collaborative trackers. In: *IEEE Conference on Computer Vision and Pattern Recognition*. (2008)